Computers & Fluids 45 (2011) 29–36

Contents lists available at ScienceDirect

Computers & Fluids

journal homepage: www.elsevier.com/locate/compfluid

Multiphysics simulations of rocket engine combustion

Yen-Sen Chen [a,*], T.H. Chou [b], B.R. Gu [b], J.S. Wu [b], Bill Wu [a], Y.Y. Lian [a], Luke Yang [a]

[a] National Space Organization, Hsinchu Science Park, Hsinchu, Taiwan
[b] Department of Mechnical Engineering, National Chiao Tung University, Hsinchu, Taiwan

ARTICLE INFO

Article history:
Received 29 June 2010
Received in revised form 23 August 2010
Accepted 14 September 2010
Available online 19 September 2010

Keywords:
Hybrid rocket combustion
N_2O–HTPB system
Radiative heat transfer
Real-fluid model
Finite-rate chemistry

ABSTRACT

Recently, the hybrid rocket propulsion has become attractive to the research community and has developed the trend to become an alternative to the conventional liquid and solid rockets. The hybrid rocket is a combination of both the solid and liquid systems with half of the plumbing of the liquid rocket but retaining its operational flexibility and avoiding the explosive nature of the solid rocket. Among available hybrid systems, the N_2O (Nitrous Oxide)–HTPB (Hydroxyl-Terminated PolyButadiene) hybrid propulsion represents the simplest but sufficiently efficient design. Unfortunately, even until now, research in developing hybrid N_2O–HTPB propulsion system still strongly depends on trials-and-errors, which are time-consuming and expensive. Thus, detailed understanding of the fundamental combustion processes that are involved in the N_2O–HTPB propulsion system can greatly impact the research community in this field. This may further facilitate the successful modeling of the combustion processes and help improving the design of N_2O–HTPB propulsion system in the future. A comprehensive numerical model with real-fluid properties and finite-rate chemistry was developed in this research to predict the combustion flowfield inside a N_2O–HTPB hybrid rocket system. Good numerical predictions as compared to experimental data are also presented.

1. Introduction

In searching for payload mass fraction performance enhancement of human's access to space technical capabilities, ramjet and scramjet (supersonic combustion ramjet) studies have been a long-term research effort in the aerospace community since the 1960s. Since the 1980s, computational modeling approaches have been gradually adopted in the aerospace community in the development of combustion devices and space launch systems. The advent of high performance computing infrastructures with improved computational techniques has turned complex numerical modeling methods, with substantial requirements in computational resources, into practical daily design analysis tools. These advancements have allowed the researchers and designers of combustion devices to simulate the combustion processes and flow physics in detailed spatial and temporal resolutions that are very difficult and expensive to obtain using experimental means. Numerical models using computational fluid dynamics (CFD) methods have been applied to liquid and solid rocket combustion systems with successful supports to the technical programs [1–6]. Recent successes in flight demonstrations of the HyShot of the University of Queensland and Hyper-X of NASA, plus the flight test of Boeing X-51 in late 2009, have promoted greater research interests in computational modeling of advanced propulsion systems. Numerical modeling efforts in simulating the supersonic combustion processes and the diagnoses of problem areas have contributed to the success of these programs.

In the recent development of space launch systems, hybrid rocket propulsion has drawn a lot of attention, especially in the civilian space tourism community, and has been demonstrated to become a viable alternative to the liquid and solid rockets, although it is still in its fledgling stage as compared to the other two types of rockets. The liquid rocket is an efficient system; however, it requires very complex and expensive plumbing systems. The solid rocket premixes the fuel and oxidizer as a grainy solid, which is dense and compact. However, it is highly explosive and lack of thrust control or termination. The hybrid rocket is a combination of both the solid and liquid systems with half of the plumbing of the liquid rockets, but retaining their flexibility of operation and avoiding the explosive nature of the solid rockets. The major advantages of the hybrid rockets include [7]: (1) safety without explosive concern, (2) flexibility in throttling and termination, (3) grain robustness without the danger of explosion originating from cracks, (4) propellant versatility, (5) temperature insensitivity to the operating chamber pressure, and (6) low cost benefiting from the safety features. Nevertheless, there are several disadvantages which include [7]: (1) low regression rate (~1 mm/s) due to the nature of the diffusion flame, (2) low bulk density (low volumetric

* Corresponding author.
E-mail addresses: yenchen@nspo.org.tw (Y.-S. Chen), chongsin@faculty.nctu.edu.tw (J.S. Wu).

0045-7930/$ - see front matter © 2010 Elsevier Ltd. All rights reserved.
doi:10.1016/j.compfluid.2010.09.010

fuel loading) due to many ports for increasing grain surface area, (3) low combustion efficiency, (4) O/F shift with burning time and location, and (5) slower transient response to throttling.

There are many types of hybrid combustion systems, in which fuel is classically a solid and the oxidizer is a liquid or gas. These include different solid fuels such as hydrocarbons (rubbers, plastics and even papers) and metals, and a wide variety of liquid oxidizers such as oxygen, hydrogen peroxide, nitric acid, nitrogen tetroxide, and nitrous oxide. Typical examples of combination of fuel and oxidizer with optimum O/F, Isp (184–326 s) and characteristic velocity (1224–2118 m/s) are discussed in Ref. [7]. Among these, most experimental data were published for propellants using LOX and HTBP with or without aluminum powder. Although no detailed data were available in the literature for the hybrid propellants using nitrous oxide as the oxidizer and HTBP related materials as the fuel, recent development of most commercial companies tends to utilize this combination, e.g. the SpaceShip One (led by Burt Rutan) which won the X Prize in September 2004 by flying up to an altitude of 100 km and landing safely back to Earth. The maximum vacuum Isp of the N_2O–HTPB propulsion system is only fair around 250 s; however, it represents the simplest one, mainly due to the self-pressurization feature of the nitrous oxide (~60 bar at room temperature), which greatly simplifies the plumbing systems. Unfortunately, even until now, research in developing the hybrid N_2O–HTPB propulsion system still strongly depends on trials-and-errors, which are time-consuming and expensive. Very few [8,9] have attempted to model complicated reactive flow phenomena of a realistic hybrid propulsion system, in which they employ an energy-balanced surface decomposition model with the assumption that decomposition of C_4H_6 (Iso-butadiene) starts at 820 K, and modeled the combustion process using some reduced reaction mechanisms with tuned rate constants.

The above modeling efforts have reached success to some extent based on fitting of experiments and numerical simulations. However, the real-fluid effects were not considered in their models. This can affect the overall flow structure in the combustion chamber, especially near the injectors, and affect the combustion processes and heat transfer characteristics, which is the key to the regression rates of the solid grain. Thus, a comprehensive numerical model is developed in this research to include the real-fluid property effects and finite-rate chemistry in the simulation of an N_2O–HTPB hybrid rocket system.

2. Method of approach

The present numerical method solves a set of governing equations describing the conservation of mass, momentum (Navier–Stokes equations), energy, species concentration and turbulence quantities. The governing equations are written as:

$$\frac{\partial \rho}{\partial t}+\frac{\partial}{\partial x_j}(\rho u_j)=0 \tag{1}$$

$$\frac{\partial \rho \alpha_i}{\partial t}+\frac{\partial}{\partial x_j}(\rho u_j \alpha_j)=\frac{\partial}{\partial x_j}\left[\left(\rho D+\frac{\mu_t}{\sigma_\alpha}\right)\frac{\partial \alpha_i}{\partial x_j}\right]+\omega_i \tag{2}$$

$$\frac{\partial \rho u_i}{\partial t}+\frac{\partial}{\partial x_j}(\rho u_j u_i)=-\frac{\partial p}{\partial x_i}+\frac{\partial \tau_{ij}}{\partial x_j} \tag{3}$$

$$\begin{aligned}\frac{\partial \rho H}{\partial t}+\frac{\partial}{\partial x_j}(\rho u_j H)=&\frac{\partial p}{\partial t}+Q_r+\frac{\partial}{\partial x_j}\left(\left(\frac{K}{C_p}+\frac{\mu_t}{\sigma_H}\right)\nabla H\right)\\&+\frac{\partial}{\partial x_j}\left(\left((\mu+\mu_t)-\left(\frac{K}{C_p}+\frac{\mu_t}{\sigma_H}\right)\right)\nabla(V^2/2)\right)\\&+\frac{\partial}{\partial x_j}\left(\left(\frac{K}{C_p}+\frac{\mu_t}{\sigma_H}\right)\left(u_k\frac{\partial u_j}{\partial x_k}-\frac{2}{3}u_j\frac{\partial u_k}{\partial x_k}\right)\right)\end{aligned} \tag{4}$$

$$\frac{\partial \rho k}{\partial t}+\frac{\partial}{\partial x_j}(\rho u_j k)=\frac{\partial}{\partial x_j}\left[\left(\mu+\frac{\mu_t}{\sigma_k}\right)\frac{\partial k}{\partial x_j}\right]+\rho(\Pi-\varepsilon) \tag{5}$$

$$\begin{aligned}\frac{\partial \rho \varepsilon}{\partial t}+\frac{\partial}{\partial x_j}(\rho u_j \varepsilon)=&\frac{\partial}{\partial x_j}\left[\left(\mu+\frac{\mu_t}{\sigma_\varepsilon}\right)\frac{\partial \varepsilon}{\partial x_j}\right]\\&+\rho\frac{\varepsilon}{k}\left(C_1\Pi-C_2\varepsilon+C_3\Pi^2/\varepsilon\right)\end{aligned} \tag{6}$$

The convection terms of the governing equations are discretized with a second-order upwind scheme. Second-order central schemes are applied to the diffusion and source terms. For complete description of the thermal environment in the combustion chamber, a radiative heat transfer model with a finite-volume integration method [1,4] is also employed in the present model. In the combustion chamber, the main participating species in the radiation model are carbon-dioxide and hot steam. For transient flow computations, an efficient second-order time-marching scheme, which has been validated for vortex shedding and transient start-up nozzle flows [6], is employed in the present study. An efficient method for comprehensive real-fluid equations of state and fluid properties is also tested for liquid propellant combustion flows. These numerical models are important for high fidelity simulations of combustion physics. They are described in the following sections.

2.1. Radiative heat transfer model

Radiation effects are important for combustion simulations when radiative participating species appear in the combustion products and in the pyrolysis gas decomposed from the solid propellant. Radiative transfer model using a finite-volume integration method is employed in this study [10,11]. Consider the radiative transfer equation (RTE) in a Cartesian coordinate system as shown in Fig. 1a. The balance of energy passing in a specified direction Ω through a small differential volume in an absorbing–emitting and scattering medium can be written as:

$$\begin{aligned}(\Omega\cdot\nabla)I_\lambda(\mathbf{r},\Omega)=&-(\kappa_\lambda+\sigma_\lambda)I_\lambda(\mathbf{r},\Omega)+\kappa_\lambda I_{b,\lambda}(\mathbf{r})\\&+\frac{\sigma_\lambda}{4\pi}\int_{\Omega'=4\pi}I_\lambda(\mathbf{r},\Omega')_\lambda(\Omega'\to\Omega)d'\end{aligned} \tag{7}$$

where the subscript λ represents the wave-number; $I_\lambda(\mathbf{r},\Omega)$ is the spectral radiative intensity, which is a function of position $\mathbf{r}$ and angular direction Ω; $I_{b,\lambda}(\mathbf{r})$ is the blackbody radiative intensity at the temperature of the medium; $\kappa\,\lambda$ and $\sigma\,\lambda$ are the spectral absorption and scattering coefficients, respectively; and $\Phi_\lambda(\Omega'\to\Omega)$ is the scattering phase function from the incoming Ω' direction to the outgoing direction Ω; and d' indicates integration over a 4π angular directions. The term on the left-hand side represents the gradient of the intensity in the direction Ω. The three terms on the right hand side represent the changes in intensity due to absorption and out-scattering, emission and in-scattering, respectively. If the wall bounding the medium emits and reflects diffusely, then the radiative boundary condition for Eq. (7) is given by

$$I_\lambda(\mathbf{r}_w,\Omega^+)=\varepsilon_\lambda I_{b,\lambda}(\mathbf{r}_w)+\frac{(1-\varepsilon_\lambda)}{\pi}\int_{\mathbf{n}\cdot\Omega^-<0}I_\lambda(\mathbf{r}_w,\Omega^-)|\mathbf{n}\cdot\Omega^-|d^- \tag{8}$$

where Ω^+ and Ω^- denote the leaving and arriving radiative intensity directions, respectively; ε_λ is the spectral wall emissivity; $\mathbf{n}$ represents the unit normal vector on the wall; d^- indicates integration over all angles of the arriving directions. Eq. (7) is a complex integro-differential equation whose exact analytical solution is only possible for very simple and specific settings. This intrinsic difficulty has resulted in the development of several approximated models. In the present model, a finite volume method (FVM) is used

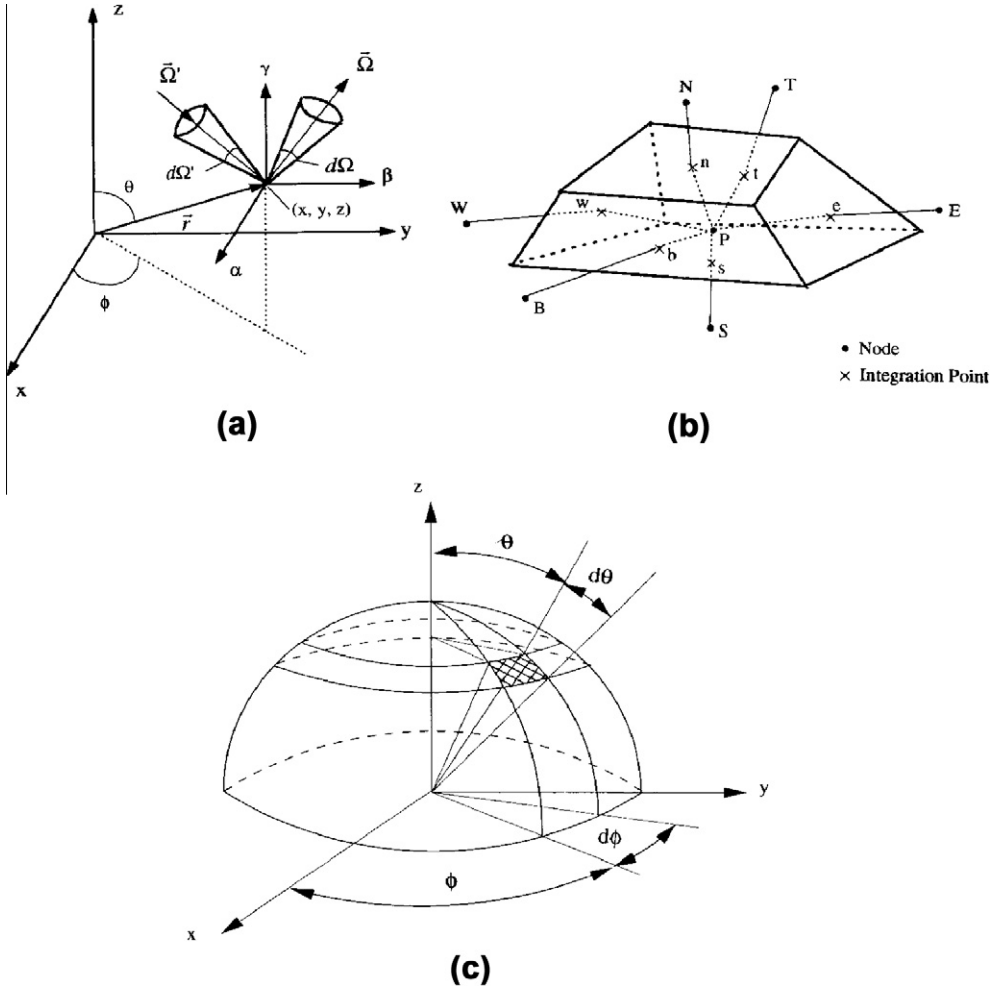

Fig. 1. (a) Coordinate system for radiative transfer equation, (b) a representative control volume, and (c) a representative control angle.

to solve the RTE and the numerical analysis procedures are briefly described here. In the following analysis, subscripts λ are dropped for the sake of brevity and they are added whenever necessary.

In the FVM, the spatial and angular domains are divided into a finite number of control volumes and control angles, respectively. Then, Eqs. (7) and (8) are integrated over each control volume and control angle. Since the FVM shares the same computational grid as the employed CFD approach, the considered spatial domain is divided into MA discrete control volumes and surfaces by a grid generator. For numerical analysis of the FVM, a representative control volume resulted from the spatial domain division is shown in Fig. 1b. By referring to the division practice for the spatial domain, the angular domain (see Fig. 1c) at a node centered in a control volume is divided into $N_\theta \times N_\phi$ = MB control angles with N_θ and N_ϕ representing numbers of control angle in polar angle θ and azimuthal angle ϕ directions, respectively. These MB discrete solid angles are non-overlapping and their sum is 4π. Unlike the selection of a quadrature scheme in the discrete ordinates method (DOM), there is no specific restriction in selecting control angles in the FVM. However, the control angles are usually chosen in a manner that best capture the physics of a given problem. This is analogous to the selection of control volumes.

Multiplying Eq. (7) by a representative control volume ΔV (Fig. 1b) and a control angle $\Delta\Omega^m$ (Fig. 1c), carrying out the integration, and transforming the left-hand side of the equation from the volume integral to a surface integral based on the divergence theorem, Eq. (7) then becomes

$$\sum_{i=e,n,t} I_i^m A_i \int_{\Delta\Omega^m} (\Omega^m \cdot n_i) d\Omega^m - \sum_{i=w,s,b} I_i^m A_i \int_{\Delta\Omega^m} (\Omega^m \cdot n_i) d\Omega^m = \left[-(\kappa+\sigma) I^m + \kappa I_b + \frac{\sigma}{4\pi} \sum_{m'=1}^{MB} \Delta\Omega^{m'} \overline{\Phi}^{mm'} I^{m'} \right]_P \Delta V \Delta\Omega^m \tag{9}$$

where the subscripts e, w, etc. indicate the values on the eastern, western, etc. surfaces of the volume; The subscript P represents the value at the central node of the control volume and A represents the control volume surface area; $\overline{\Phi}^{mm'}$ is the averaged scattering phase function from the control angle $\Delta\Omega^{m'}$ to the control angle $\Delta\Omega^m$. Dividing Eq. (9) by $\Delta\Omega^m$, we have

$$\sum_{i=e,n,t} I_i^m A_i \overline{D}_i^m - \sum_{i=w,s,b} I_i^m A_i \overline{D}_i^m = [-(\kappa+\sigma) I^m + \kappa I_b + \frac{\sigma}{4\pi} \times \sum_{m'=1}^{M} \Delta\Omega^{m'} \overline{\Phi}^{mm'} I^{m'}]_P \Delta V \tag{10}$$

where

$$\overline{D}_i^m = n_i \cdot \overline{\Omega}^m = \frac{1}{\Delta\Omega^m} \int_{\Delta\Omega^m} (\Omega^m \cdot n_i) d\Omega^m \tag{11}$$

In Eq. (11), $\overline{D}_i^m$ is the product of a surface unit normal vector and the averaged intensity direction $\overline{\Omega}^m$. To close the above equation, relations are needed between the intensities on the control volume surfaces and the nodal intensities. One appropriate closure relation for complicated geometries is based on the step scheme,

which sets the downstream surface intensities equal to the upstream nodal intensities. Use of the step scheme avoids the negative intensities, overshoots, and undershoots which may occur in other radiation schemes such as the diamond scheme, and positive scheme. Furthermore it has much less connection with the neighboring nodes, and thus it is particularly suitable for parallel computation. The effect of the step scheme on communication costs is not significant. The final discretized equation for the FVM can be written as

$$a_P^m I_P^m = a_E^m I_E^m + a_W^m I_W^m + a_N^m I_N^m + a_S^m I_S^m + a_T^m I_T^m + a_B^m I_B^m + b^m \tag{12}$$

where the intensities with the subscripts E, W, etc. denote the eastern, western, etc. nodal intensities, and

$$a_P^m = \sum_{i=e,n,t} \max(A_i \overline{D}_i^m, 0) - \sum_{i=w,s,b} \min(A_i \overline{D}_i^m, 0) + \Delta V(\kappa + \sigma) \tag{13a}$$

$$a_I^m = -\min(A_i \overline{D}_i^m, 0) \quad i = e,n,t \text{ and } I = E,N,T \tag{13b}$$

$$a_I^m = \max(A_i \overline{D}_i^m, 0) \quad i = w,s,b \text{ and } I = W,S,B \tag{13c}$$

$$b^m = \Delta V \left[\kappa I_b + \frac{\sigma}{4\pi} \sum_{m'=1}^{MB} \Delta\Omega^{m'} \overline{\Phi}^{mm'} I^{m'} \right]_P \tag{13d}$$

The preceding discretization is carried out along only one control angle at a node. The same procedure should be applied to all of the MB control angles at all of the MA nodes. This forms MA×MB systems of non-symmetric algebraic equations. A solution of these equations only represents radiative contribution at a single wave number. The radiative divergence is the quantity used in the energy equation and it should consist of radiative contributions from all wave numbers. The radiative divergence is expressed in terms of the radiative intensities as

$$\begin{aligned} \nabla \cdot q_r &= \int_0^\infty \left[-\kappa_\lambda \int_0^{4\pi} I_\lambda d\omega + \kappa_\lambda \int_0^{4\pi} I_{b,\lambda} d\omega \right] d\lambda \\ &= \int_0^\infty \left[4\pi\kappa_\lambda I_{b,\lambda} - \kappa_\lambda \sum_{m=1}^{MB} I_\lambda^m \Delta\Omega^m \right] d\lambda \end{aligned} \tag{14}$$

A typical radiatively participating gas consists of many lines whose absorption coefficients vary rapidly with wave number. Thus, it becomes a very difficult and time-consuming to evaluate the radiative properties over the actual band contour and include them into the RTE. To avoid this difficulty, the spectrum can be divided into MC bands and the radiative properties are assumed constant over each band. The integrated quantity in Eq. (14) is found as the summation over all bands of the individual contribution for each band, that is,

$$\nabla \cdot q_r = \sum_{j=1}^{j=MC} \left[4\pi_{\lambda_j} \kappa_j I_{bj} - \kappa_j \sum_{m=1}^{MB} I_{\lambda_j}^m \Delta\Omega^m \right] \Delta\lambda_j \tag{15}$$

The above approach to the spectral problem essentially corresponds to the spectral discretization and it represents a good compromise between accuracy and computational time. The number of MC can be changed from one (gray gas model) to several hundred (narrow band model). Obviously, the use of higher MC number provides more accurate results.

2.2. Transient time-marching scheme

In the present numerical model, the temporal terms of the transport equations are modeled with a second-order backward difference scheme. There are two ways of performing time-marching procedures. First, the momentum, energy and pressure-correction equations are grouped together within an iteration loop and drive to convergence for each time step. Although the transient sub-iteration method described in the previous section is accurate for transient flow applications, it requires many sub-iterations (more for highly dynamic cases) to advance one time step, especially for low-speed flows. In order to save computational effort in transient flow applications, this sub-iteration algorithm can be replaced with a more efficient method, such as the operator splitting technique [12–14]. This method consists of a predictor step plus two corrector steps to drive the discretization errors to second-order accuracy.

Testing of the transient model is described in the following sections. Some test cases are identified for time accurate modeling and data comparisons. They are: (1) the laminar and turbulent vortex shedding flows behind a circular cylinder; and (2) unsteady multi-species flows past a circular cylinder with and without chemical reactions. The mesh and test conditions for these cases are prepared with initial uniform flow conditions. Proper time step sizes were selected for good solutions of these transient cases. Knowing the cycle time period from the experimental data, the computational time step size is then determined such that there are at least 200 time steps within one cycle. For cases without experimental data a priori, grid and time-step convergence tests are required numerically. This is a good guideline based on previous experience although some adjustment may be needed for special cases with multiple dominant frequencies and/or frequency modulations.

2.3. Real-fluid combustion modeling

In order to perform analyses of phase change phenomena in cavitation, liquid sprays or cryogenic fluid flows, real-fluid thermal and caloric equations of state (EOS) were developed for use with the present CFD code. The HBMS equations of state [15–17] were chosen for this purpose. Thermal and caloric equations of state, vapor pressure, heat of vaporization, surface tension, and transport properties are modeled with the equations of state proposed by Hirshfelder et al., as employed by Dooley [18] and Anon. [19] (we term these the HBMS equations of state), and with conventional correlations [20] for the other properties. The property correlations used were not chosen for their absolute accuracy, but for their validity over a wide range of temperatures and pressures and for requiring a minimum of data to describe a particular species. These correlations are explicit in density and temperature. These equations are:

HBMS thermal equation of state:

$$\frac{P}{P_c} = \sum_{j=1}^{4} T_r^{j-2} \sum_{i=1}^{6} B_{ij} \rho_r^{i-2}; \quad T_r = \frac{T}{T_c}; \quad \rho_r = \frac{\rho}{\rho_c}$$

HBMS caloric equation of state:

$$\frac{H - H_0}{RT} = Z_c \int_0^{\rho_r} \left[\frac{P}{T_r} - \left(\frac{\partial P}{\partial T_r} \right)_{\rho_r} \right] \rho_r^{-2} d\rho_r + Z_c \frac{P}{\rho_r T_r} - 1$$

These equations are not only of sufficiently high order that properties are accurately predicted for a wide range of conditions, but component sub-models may be easily modified. In this instance, the vapor pressure curve and the liquid phase density correlations were improved over the original HBMS formulations. Other equations of state were considered, but were found not to be as satisfactory as the HBMS equations.

Multi-component mixtures were treated by adding partial specific volumes or pressures. The partial volume methodology is essential to improve the accuracy of the prediction when a small amount of multi-component vapor and a large amount of liquid are present at the same point. The fluid property routines also

include correlations for the transport properties. This was convenient since much of the methodology was similar.

2.4. Real-fluid model computational speed

In assessing the computational overhead associated with using the real-fluid property sub-model, numerical experiments of simulating some converging–diverging pipe flows with ideal gas and liquid oxygen working fluids were conducted to quantify the CPU time overhead when the real-fluid model is activated. The results show an overall CPU time increase of about 85% for the real-fluid cases. These results indicate that there are rooms for improvement in order to enhance the turnaround time of running multi-phase flow problems. To improve the computational efficiency, a real-fluid table lookup procedure was developed for the present CFD model. This method is much more efficient than the original real-fluid model which involves the inversion of curve-fit data describing the equation of state. In average, the real-fluid table lookup model is only 15% slower than its ideal-gas counterpart. This means about 70% saving in CPU time with the real-fluid table lookup method.

2.5. Multi-species mixture implementation

For general applications of the present table-lookup real-fluid model, one must consider the conditions of multi-species mixing processes. To streamline the modeling approach for better performance in terms of computational efficiency and program coding clarity, functions for calculating enthalpy, specific heat and density are created based on the current code structure of the present CFD model. These new functions now consist of extra sections for the real-fluid properties based on the local pressure, temperature and species concentrations. The table lookup section is activated when the temperature is lower than the value that divides the real-fluid and perfect gas properties. Within the table lookup section, the pressure level is first used to define a property curve based on the database provided. Then, the fluid property is obtained through interpolation based on this new curve.

3. Real-fluid model combustion test

A benchmark LOX/GH2 single-injector combustor test case of DLR, Lampoldshausen, Germany (RCM2), is simulated to validate the current real-fluid table lookup model. This is one of the benchmark cases presented in the 2nd international workshop on rocket combustion modeling [21]. The test conditions and geometry of this case are summarized as:

chamber pressure = 1 MPa;
LOX mass flow rate = 0.05 kg/s (at 85 K);
GH_2 mass flow rate = 0.0237 kg/s (at 287 K);
chamber geometry = 0.05 m $\times$ 0.05 m square;
chamber length (injector to throat) = 0.472 m;
LOX inner tube diameter = 0.005 m;
GH_2 annulus duct width = 0.0032 m;
injector lip thickness = 0.0003 m;
nozzle throat diameter = 0.015 m.

Computational model for this case includes an axisymmetric mesh with a grid size of 18,715, a time step size of 1.0E−06 s, real-fluid table for LOX, a 6-species and 9-reaction chemistry system and a 1500 K spark region near the injector lip region. 35,000 time steps were required for a converged solution. Most of the CPU time was spent for chamber pressure buildup to balance the overall mass conservation of the system (i.e. chamber pressure is reduced initially and then gradually increased after the flame zone is established). Methods for speeding up the pressure buildup process for this type of problem are important for better overall efficiency in computational efforts. Multi-grid matrix solver has been shown to be effective in this aspect through the reduction of long wave errors.

Another conclusion obtained in this case study is that the current real-fluid table model only cost about 15% more CPU time per step than the original ideal-gas model. The extra CPU time is spent for table lookup of the species properties and a searching procedure to obtain the mixture temperature. This also demonstrates a substantial improvement in computational efficiency over the original real-fluid model. Fig. 2 shows the flowfield solutions of the RCM2 test case. The predicted shape of the flame zone is in close resemblance with the flame Abel-transformed emission image of the experiment, which is the same result as the original real-fluid model [21].

4. Hybrid rocket combustion experimental setup

A typical hybrid rocket hot-fire testing rig is schematically shown in Fig. 3. The facility includes a horizontal motor casing made of stainless steel, a pressurized vertical tank containing nitrous oxide, and a solenoid or pneumatic throttling valve between the motor and the tank. This throttling valve is used to start, partially open, and stop of nitrous oxide flow. Preliminary design of the horizontal motor casing along with several locations of instrumentation is incorporated. There is a pintle-type injector at the end of plumbing from the tank, which is used to inject the liquid nitrous oxide into the pre-combustion chamber. Note the liquid nitrous oxide will become mainly gaseous nitrous oxide as it enters the pre-combustion chamber because of the lower pressure as compared to the saturation pressure of the nitrous oxide.

Both the pressures in the pre- and post-combustion chambers are measured using pressure transducers. Measurement of the pressure in the post-combustion chamber requires cooling of the combusted gases through long metal tube to protect the pressure transducer. Temperatures in the pre- and post-combustion chambers are measured using S-type thermocouples. In addition, only temperatures inside the HTPB grain are measured since the temperature in the central port is too high to measure using thermocouples. All data are acquired and processed using a computerized data acquisition system (National Instruments, Inc.) through a well-known LabView software. This is an effective, reliable and low-cost experimental setup.

5. Hybrid rocket combustion testing and numerical modeling

The present hybrid rocket combustion model include a 580 mm combustion chamber with the design of forward-end and aft-end mixing chambers. A simple convergent–divergent conical nozzle is attached to the end of the combustion chamber. A single-port simple solid grain of HTPB is cast in two sections and assembled into a single segment through bonding. To boost the mixing efficiency, a mixing enhancer (patent pending) is also installed near the forward corner of the solid grain. A pintle-type injector made of stainless steal is employed for steady injection of the N_2O oxidizer. The nitrous oxide tank upstream of the injector and control valve is setup in a vertical position. Due to the properties of the oxidizer and the absence of thermal control for the oxidizer tank and without using a pressurant tank upstream, the injection flow rates of this pressure-fed injection system depend directly on the temperature of the environment. A small pyro grain is attached to the forward face of the solid grain, which is ignited at engine

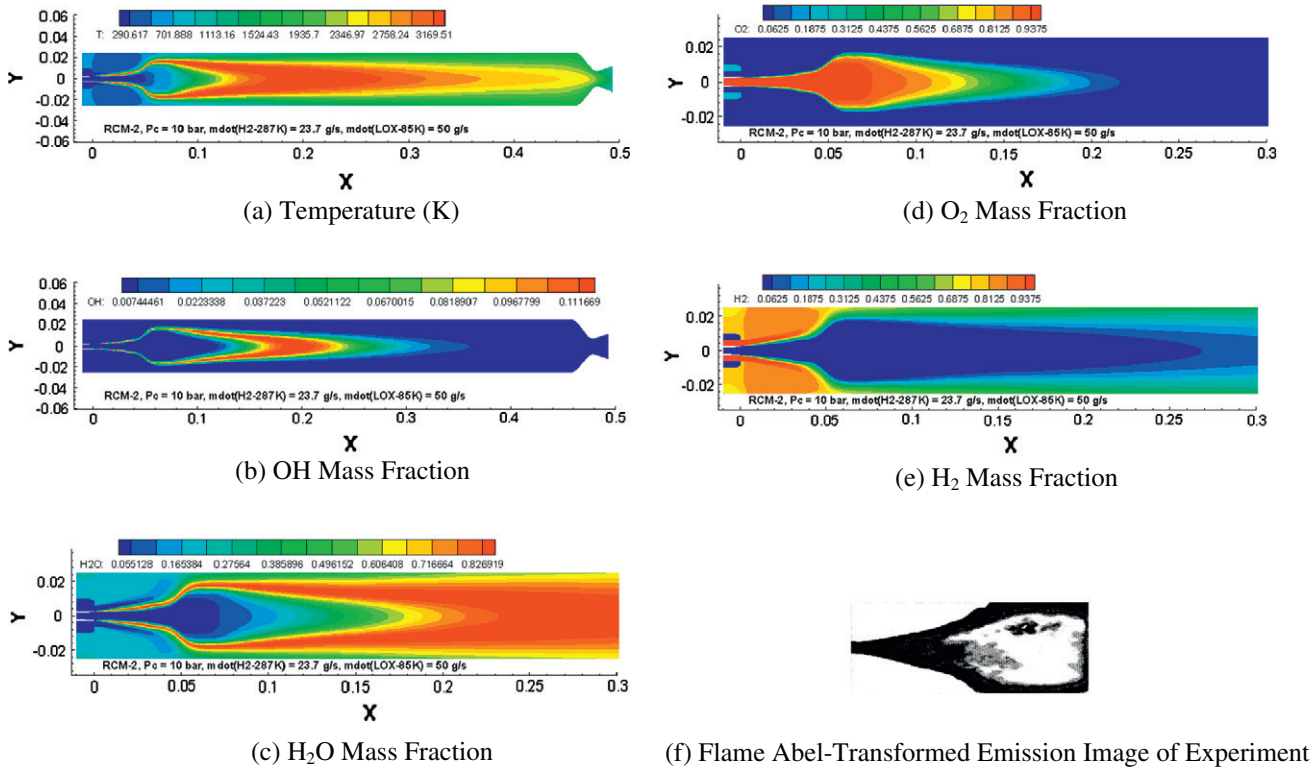

Fig. 2. Predicted flowfield of the RCM2 test case with the current real-fluid-table combustion model.

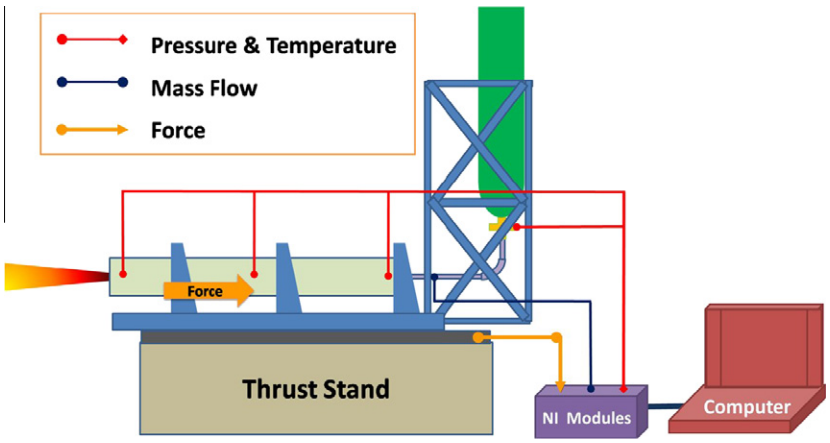

Fig. 3. Experimental apparatus of the static burn test of a hybrid rocket motor.

start-up to melt the HTPB solid and start the combustion process after the N_2O control valve is commanded to open.

Typically, a hot-fire test of this experiment runs between 15 and 20 s. During the test, motor thrust, chamber pressures and HTPB port temperatures are measured. The oxidizer flow rates and the regression rates of the solid grain are obtained through post-processing after the hot-fire tests. Overall, the experimental data show that the averaged solid regression rate is around 1 mm/s for the current design. The measured specific impulse, sea-level Isp, of the motor with the mixing enhancer is around 213 s (or vacuum Isp of 222.18 s). From previous experimental study without the mixing enhancer, the measured sea-level Isp was around 178 s for a similar motor.

To model this test case, an axisymmetric mesh system with 91,960 elements is generated to model the geometry of the combustion chamber, pintle injector, solid grain and the conical nozzle. The mixing enhancer is not modeled in the present simulation due to its 3-D complexity, which will be explored in future research. A real-fluid property database is created to represent the nitrous oxide fluid in the numerical model. A 13-species, 17-reaction finite-rate chemistry model is employed to model the combustion process. This includes the thermal decomposition of the oxidizer, pyrolysis of the HTPB solid and combustion of the gaseous mixture. A radiation model with finite-volume integration method is used to calculate the radiative heat transfer effects. The turbulence fields are predicted with an extended two-equation model [12,13]. The total pressure (50 ATM) and total temperature (283 K) boundary conditions are imposed at the injector inlet with the consideration of estimated total pressure losses between the tank and the injector inlet. However, this setup still can not represent the true test

conditions because the real inlet conditions are transient in nature. During the test, the tank pressure and temperature are reduced rapidly due to high flow rate and the expansion effects. Therefore, in the present model, we compare the numerical predictions to the test data when the oxidizer injection stays in the liquid phase, i.e. between 2 and 7 s after ignition.

The numerical simulation takes 80,000 time steps with 1 μs time step size to obtain a quasi steady-state solution of the flow-field. Fig. 4 shows the predicted hybrid rocket motor combustion flowfield using the present numerical model. It is clear that well-organized shear-layer oscillation structure, similar to the Taylor–Goertler type instability effects of thin shear layers, is predicted for the injection system. This oscillation is then coupled with the oxidizer decomposition process and the flame along the solid grain surface. Clearly, the axisymmetric simplification of the present model can not represent the real physics of shear layer instabilities.

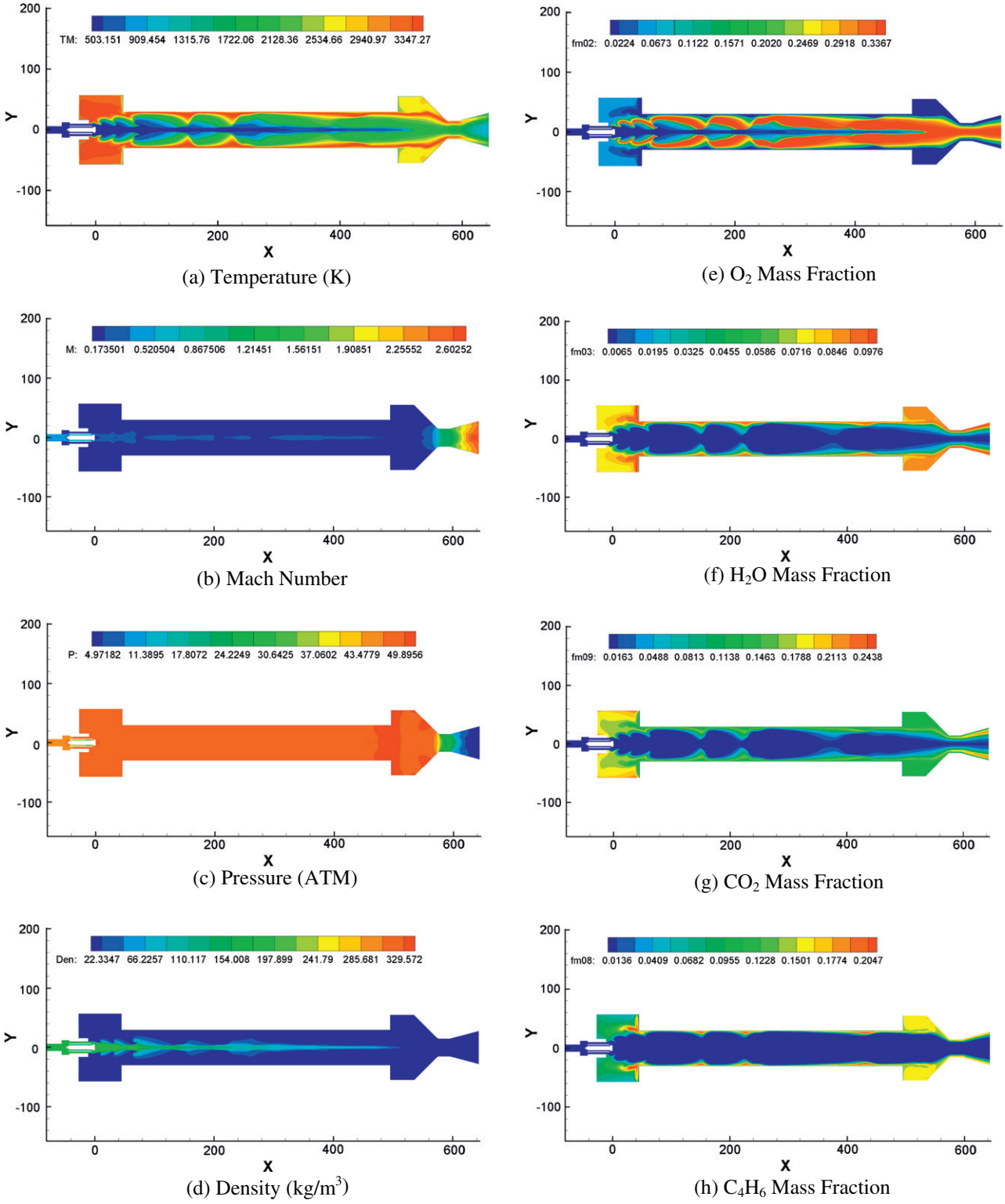

Fig. 4. Computational results of the static burn test of a N_2O–HTPB hybrid rocket motor.

And, it is plausible that the oxidizer evaporation may also contribute to the oscillation of the predicted flowfield. From the density plot of Fig. 4, a long liquid (or high density fluid) core is clearly shown in the predicted flowfield. This indicates that further improvement in the injector design or mixing enhancement method in the chamber is required in order to increase the overall performance of this combustion system. The predicted averaged sea-level Isp is 181.2 s (or vacuum Isp of 191.18 s), which is lower than the measured data as expected due to the fact that a mixing enhancer is not present in the numerical model.

To increase computational efficiency of the present complex model with multiphysics capabilities, parallel computation is employed on an IBM cluster computer system. Classes of 8-CPU, 32-CPU and 64-CPU were tested in the study. Results show parallel efficiency of around 0.97 (7.76 times speed up), 0.86 (27.52 times speed up) and 0.71 (45.44 times speed up), respectively, for these three classes of runs. The sharp decrease in parallel efficiency for the 64-CPU cases is due to the reduced mesh size for each processor and increased communication between processors.

6. Conclusions

In this study, we have developed a comprehensive numerical model for predicting the combustion flowfield of a hybrid rocket motor. A real-fluid property model has been employed for accurate description of the thermal-fluid environment of the N_2O–HTPB hybrid rocket combustion system. In the real-fluid property modeling, a table lookup method has been implemented in the present study to improve the computational efficiency for realistic flow physics representation. The improved model has shown good solutions as it is applied to a liquid rocket engine combustion test case conducted at DLR, Germany. The overall improvement in computational efficiency for real-fluid combustion simulations is about 70%. This provides substantial saving in computational efforts for the simulations of combustion processes with real-fluid properties.

The experimental investigation of the N_2O–HTPB hybrid rocket combustion system has demonstrated the effective, reliable and low-cost setup of the present design. The measured motor performance data is provided to anchor the numerical model developed in the present study. The present numerical solutions have shown interesting flowfield in the hybrid motor combustion chamber. The predicted quasi steady-state specific impulse shows close comparison to the test data. Nevertheless, the simulation is still a 2-D axisymmetric representation of the experiment, which can not simulate the true mixing process of the shear layer of the oxidizer injection. For future study, full 3-dimensional simulations in transient process will be modeled to include the effects of realistic turbulence mixing downstream of the injector.

Acknowledgements

This work is supported by the Sounding Rocket Program of the National Space Organization of the National Applied Research Laboratory. The computational resources and services are provided by the National Center for High-performance Computing of the National Applied Research Laboratory.

References

[1] Chen YS, Liu J, Zhang S, Mallapragada P. An integrated tool for launch vehicle base-heating analysis. Final report, NAS8-00002. Huntsville: Engineering Sciences, Inc., AL; 2001.
[2] Liaw P, Shang HM, Chen YS. Particulate multi-phase flowfield calculation with combustion/breakup models for solid rocket motor. AIAA-94-2780, 30th AIAA/ASME/SAE/ASEE joint propulsion conference, Indianapolis, IN, June 27–29, 1994.
[3] Chen YS, Zhang S, Liu J. Stage separation performance analysis project. Final report, H-34345D. Huntsville, AL: Engineering Sciences, Inc.; 2002.
[4] Wang TS, Chen YS, Liu J, Myrabo LN, Mead Jr FB. Advanced performance modeling of experimental laser lightcraft. J Propul Power 2002;18(6):1129–38.
[5] Wang TS. Multidimensional unstructured-grid liquid rocket engine nozzle performance and heat transfer analysis. J Propul Power 2005;22(1):78–84.
[6] Wang T-S. Transient 3-D analysis of nozzle side load in regeneratively cooled engines. AIAA paper 2005-3942, 41st AIAA/ASME/SAE/ASEE joint propulsion conference, Tucson, Arizona; 2005.
[7] Fundamentals of hybrid rocket combustion and propulsion. In: Chiaverini MI, Kuo KK, editors. Progress in astronautics and aeronautics, vol. 218; 2007.
[8] Farmer RC, Cheng GC, Jones SH, Arves JP. A practical CFD model for simulating hybrid motors. JANNAF 35th combustion, airbreathing propulsion, and propulsion systems hazards subcommittee joint meeting, Tucson, AZ, 1998.
[9] Farmer RC, Cheng GC, Metshc TH. Analysis of steady and unsteady hybrid combustion. JANNAF propulsion & joint subcommittee meeting, Albuquerque, NM, 1996.
[10] Liu JW, Chen YS. Parallel simulation of radiative heat transfer using an unstructured finite-volume method. Numer Heat Transf B 1999;36:115–37.
[11] Liu JW, Chen YS. Development of an unstructured radiation model applicable for two-dimensional planar, axisymmetric and three-dimensional geometries. J Quant Spectrosc Radiative Transf 2000;22:17–33.
[12] Kim YM, Chen CP, Ziebarth JP, Chen YS. Prediction of high frequency combustion instability in liquid propellant rocket engines. AIAA 92-3763, AIAA/SAE/ASME/ASEE 28th joint propulsion conference and exhibit, Nashville, TN, July 6–8, 1992.
[13] Chen YS, Cheng GC, Farmer RC. Reacting and non-reacting flow simulation for film cooling in 2-D supersonic flows. AIAA 92-3602, AIAA/SAE/ASME/ASEE 28th joint propulsion conference and exhibit, Nashville, TN, July 6–8, 1992.
[14] Wang TS, Chen YS. Unified Navier–Stokes flowfield and performance analysis of liquid rocket engines. J Propul Power 1993;9(5):678–85. September–October.
[15] Uyehara OA, Watson KM. A universal viscosity correlation. Natl Petrol News 1944:R-714–22.
[16] Maxwell JB. Data book on hydrocarbons. NY: Van Nostrand Co.; 1950.
[17] Farmer RC, Cheng GC, Chen YS. Parallel processing of the 3D3P codes. SECA-FR-02-02, SECA, Inc., Huntsville, AL, 2002.
[18] Dooley RB. The international association for the properties of water and steam. September 1997 release. See also 2001 and 2003 releases available on IAPWS web site.
[19] Anon. ASME steam properties for industrial use. NY: ASME Press; 1998.
[20] Dean LE, Shurley LA. Characteristics of RP-1 rocket fuel. Aerojet general corporation, technical report TCR-70, 1957.
[21] Cheng G, Farmer RC, Chen YS. CFD simulation of liquid rocket engine injectors, part 2: simulations of the RCM-2 experiment. 2nd international workshop, rocket combustion modeling, Lampoldshausen, Germany, March 25–27, 2001.